

Phase-field model of oxidation: KineticsKyoungdoc Kim,¹ Quentin C. Sherman,¹ Larry K. Aagesen,² and Peter W. Voorhees^{1,*}¹*Department of Materials Science and Engineering, Northwestern University, Evanston, Illinois 60208, USA*²*Fuels Modeling and Simulation Department, Idaho National Laboratory, P.O. Box 1625, Idaho Falls, Idaho 83415, USA*

(Received 9 September 2019; accepted 27 January 2020; published 24 February 2020)

The kinetics of oxidation is examined using a phase-field model of electrochemistry when the oxide film is smaller than the Debye length. As a test of the model, the phase-field approach recovers the results of classical Wagner diffusion-controlled oxide growth when the interfacial mobility of the oxide-metal interface is large and the films are much thicker than the Debye length. However, for small interfacial mobilities, where the growth is reaction controlled, we find that the film increases in thickness linearly in time, and that the phase-field model naturally leads to an electrostatic overpotential at the interface that affects the prefactor of the linear growth law. Since the interface velocity decreases with the distance from the oxide vapor, for a fixed interfacial mobility, the film will transition from reaction- to diffusion-controlled growth at a characteristic thickness. For thin films, we find that in the limit of high interfacial mobility we recover a Wagner-type parabolic growth law in the limit of a composition-independent mobility. A composition-dependent mobility leads to a nonparabolic kinetics at small thickness, but for the materials parameters chosen, the deviation from parabolic kinetics is small. Unlike classical oxidation models, we show that the phase-field model can be used to examine the dynamics of nonplanar oxide interfaces that are routinely observed in experiment. As an illustration, we examine the evolution of nonplanar interfaces when the oxide is growing only by anion diffusion and find that it is morphologically stable.

DOI: [10.1103/PhysRevE.101.022802](https://doi.org/10.1103/PhysRevE.101.022802)**I. INTRODUCTION**

Oxidation or corrosion occurs when most engineering metals are exposed to air or oxidizing environments. The corrosion process causes unwanted loss of metal from an engineering component via chemical reactions in which a metal atom loses one or more electrons to form an oxide. However, once the metal surface is covered with a continuous layer of metal oxide, molecular oxygen in the air can no longer directly reach the base metal. Continued oxidation must therefore occur via ionic diffusion through the oxide layer. Thus, oxides with slow ionic diffusion kinetics, which impede continued oxide growth, are essential for designing corrosion resistant alloys. The oxidation process generally involves complex coupling between chemical reactions, mass transport, and electrostatic interactions due to the ionic nature of the metal oxide. Mass transport normally involves migration of ionic defects (vacancies and interstitials) and electronic defects (electrons and holes). Oxide growth mechanisms are determined by the oxide defect structure, cation, or oxygen transport. For example, the nickel oxide forms at the gas-oxide interface by cation transport during outward growth with a stationary nickel-nickel oxide interface [1]. On the contrary, the inward oxidation by oxygen is dominant in aluminum oxide, leading to oxide-metal interface motion in the early stage of oxidation [2], or both cation and oxygen transport through oxide [3]. The growth of chromium oxide is also controlled by anionic transport via oxygen vacancies [4].

Oxidation growth kinetics has been extensively examined both theoretically and experimentally. Long-term thermal

oxidation is generally well described by the parabolic growth law of Wagner [5] in the thick film limit, thickness typically more than 1 μm . The driving force for oxidation that leads to the parabolic growth law is a fixed chemical potential difference at the two reaction boundaries in one dimension [6]. Wagner theory assumes that oxidation is a diffusion-limited process, that the interface is in local equilibrium, and that the bulk oxide is charge neutral. The assumption of charge neutrality in the bulk oxide relies on the fact that the film thickness L is large compared to the electronic screening length [7] or Debye length L_D [8] of the oxide, defined as $L_D = \sqrt{\epsilon^O k_B T / q^2 c_d}$ where c_d is the native charged defect density in the oxide, ϵ^O is the permittivity of the oxide, and q is the elementary charge. k_B and T are Boltzmann's constant and temperature, respectively. In the case when the film thickness is extremely thin, typically less than 20 nm, the diffusion-limited growth law and charge neutrality assumption cannot generally be assumed valid. Cabrera and Mott's theory [9] adopts the concept of ionic drift (e.g., cation transport) through the oxide, driven by the presence of a large constant electric field established by an electron tunneling current, to arrive at an inverse logarithmic growth law. In general, the range of validity of Cabrera and Mott theory and Wagner theory can be well defined in terms of the Debye length. The general description of Wagner theory and Cabrera and Mott theory has been described in greater detail by Atkinson [10].

There have been many efforts to understand the oxide growth process in between the thick and thin film limits. For example, there is a transition from a linear to a parabolic growth law during the early stage of thermal oxidation of silicon, consistent with a transition from reaction- to diffusion-controlled growth, as found by Deal and Grove [11]. Also, the same transition kinetics was observed in chromium oxide

*p-voorhees@northwestern.edu

growth by anion diffusion under $\text{H}_2\text{O}-\text{H}_2$ gas mixtures [12]. However, the general description is still incomplete in the intermediate length scales due to complexities of electrostatic effects during the oxidation. For example, corrosion resistant oxide phases, such as Cr_2O_3 and Al_2O_3 , have Debye lengths on the order of tens of nanometers due to low native defect concentrations [10]. This means that the presence of space charge needs to be considered until the oxide thickness is on the order of 100 nm or greater. Since the transition in the kinetics of oxidation with increasing oxide film thickness is a complicated problem with chemical and electrostatic interactions, we need to adopt numerical simulation or calculation methods using computational tools.

The phase-field method has been widely used as a diffuse-interface approach to describe the complex and nonlinear nature of microstructure evolution with time [13,14]. In this approach, we can avoid the mathematically difficult problems of applying boundary conditions at a moving interface and explicitly tracking the interface motion can be avoided. Previously, Wen *et al.* [15] proposed a phase-field model to simulate corrosion kinetics under oxidation and sulfidation. The model assumes diffusion without considering the effects of electrostatic energy during inward oxidation in an oxide-metal system. Cheng *et al.* [16] focused on that a transition from a reaction- to diffusion-controlled growth occurs when film thickness is on the order of the Debye length and showed that their model reproduces a linear to parabolic growth rate law similar to that in [11]. Cheng *et al.* chose Cahn-Hilliard (C-H) evolution equations [17,18] for a phase-field variable including an additional source term for the oxide production. This is the so-called Cahn-Hilliard-reaction (CHR) equation [19] for reaction-diffusion phenomena. Specifically, Cheng *et al.* use a free energy description of a phase-field variable without electrostatic potential contributions, and separately solved diffusion equations for defects along with Poisson's equation. Thus, the phase-field variable is decoupled from the electrostatic potential. The well-known Butler-Volmer kinetics in electrochemistry was not considered in the source term that is responsible for interfacial motion. Thus, an electrostatic overpotential at the interface was not observed, which is an important physical effect during reaction-limited growth. The surface charging effect due to oxygen reduction was also not considered, and the study was also limited to oxidation kinetics in one dimension. We relax these assumptions in our work below.

Guyer *et al.* [20,21] developed a “complete” phase-field model of an electrochemical system consisting of an electrode and electrolyte and determined the equilibrium state and evolution process in one dimension. Guyer *et al.* added Poisson's equation as a constraint when taking the variational derivatives needed to derive the evolution equations for the phase-field method. The advantage of this approach over an explicit solution of Poisson's equation is that it ensures that Poisson's equation holds at all points in the computational domain. Thus, this method gives the dependence of electrostatic potentials on defect concentrations very accurately. This is needed since small changes in defect concentrations produce large changes in the potential. However, it is very challenging to implement Guyer's method because the evolution equations are very stiff, rendering even one-dimensional simulations

very difficult. It makes it even more difficult to follow the evolution of nonplanar interfaces in higher-dimensional simulations [22]. Thus, most oxidation simulations do not employ the model of Guyer *et al.* and account for the electrostatic double layer [15,22–25]. As a result, it is difficult to make predictions for thin films below the Debye length where the electrostatic potential is important. Recently, Sherman and Voorhees [26] developed a phase-field model of a metal-oxide interface that is coupled to the electrostatic double layer at the interface using the approach of Guyer *et al.* to study the equilibrium state for thick and thin films. This phase-field model was validated using the Gouy-Chapman model for the electrostatic double layer [26]. However, the study was still limited to one dimension, and only computed the equilibrium state of the oxide-metal system. Thus, it is not possible to account for the effects of electrostatics on growth, or follow the evolution of nonplanar interfaces, such as those commonly seen experimentally. To address this challenge, we use a finite element method implemented in the Multiphysics Object Oriented Simulation Environment (MOOSE) framework. We show that the Lagrangian method of Guyer *et al.* is practicable in two dimensions with electrostatic double layers and can be used to follow the evolution of both one-dimensional (1D) and two-dimensional (2D) interfaces for long times. As a result, it is now possible to both examine the effects of the double layer on the kinetics of oxidation as well as follow the evolution of nonplanar interfaces.

Most kinetic studies of oxidation have been performed in one dimension and thus assume that the oxide-metal interface is planar. Similar to the morphological changes of phase boundaries during solidification, it is common to observe nonplanar oxide-metal interfaces [27], thus invalidating assumption of planarity. These nonplanar morphologies have important technological implications since the amplitude of the interfacial perturbations can increase in time leading to a breakdown of the oxide film. Morphological instabilities can be driven by electric, magnetic, or elastic fields and compete with a stabilizing influence of interfacial energy [28–33]. A linear stability analysis has often been used for understanding morphological instability, for example, the evolution of the oxide-metal interface was analyzed during aluminum oxide growth by oxygen diffusion in the Ni-Al system [2]. However, linear stability theory does not hold when amplitudes of perturbations are comparable to film thickness especially, for example, in the early stage of oxidation, during the inward growth of aluminum oxide [34]. Here, we analyze the morphology of the interface during oxidation in two dimensions and the nonlinear regime where the amplitude of perturbations is a similar order of magnitude of the Debye length and the wavelength of the perturbation, using the phase-field model. Our approach here can facilitate multidimensional oxidation studies and ultimately can significantly impact understanding oxidation kinetics in the future.

II. MODEL DESCRIPTION AND FORMULATION

A. Oxide film growth in thick film limit

We develop an analytical description of oxide growth to compare with the result of our phase-field simulations in

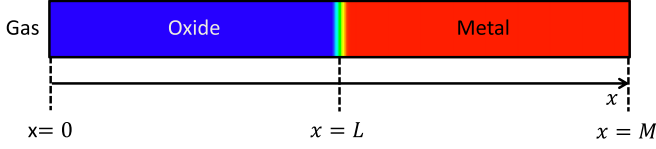


FIG. 1. Schematic of the gas-oxide-metal system used in this work. The dotted lines represent gas-oxide interface ($x = 0$), oxide metal interface ($x = L$), and metal edge ($x = M$), respectively.

the thick film limit where charge neutrality holds in bulk oxide and the mobility of each species is independent of concentration. Using the crystallography and charge neutrality of the oxide, there are two diffusion fluxes \mathbf{J}_i of charged specie i through oxide film that control the growth of oxide,

$$\mathbf{J}_i = -M_i \nabla \bar{\mu}_i^O = -M_i \nabla (\mu_i^O + q_i F \psi^O) \quad \text{for } i = v, e, \quad (1)$$

where M_i , $\bar{\mu}_i^O$, and $\mu_i^O(c_i)$ are the defect mobility, electrochemical potential, and chemical potential of species in oxide film. The subscript i is anion oxygen vacancy or electron. The superscript O represents the oxide phase. q_i is the charge number of the species. F is Faraday's constant and ψ^O is the electrostatic potential. The rate of change of the concentration field, assuming that the mobilities are not a function of concentration, is

$$\frac{\partial c_i}{\partial t} = -\nabla \cdot \mathbf{J}_i = M_i \nabla^2 \bar{\mu}_i^O \quad \text{for } i = v, e, \quad (2)$$

where c_i are the defect concentrations of anion vacancy v or electron e . Here, we assume a concentration-independent mobility, which is one of the cases considered in the phase-field model. Equation (2) can be simplified in the quasistationary limit, in which the diffusion field is relaxed on the timescale of the interface motion and the concentration field is given by a solution to Laplace's equation for the electrochemical potentials, as is typically assumed in analytical models of oxide growth. Thus, the diffusion flux must be constant across the oxide in one dimension. This implies that the gradient in the electrochemical potential is $\Delta \bar{\mu}_i^O/L$, where

$$\Delta \bar{\mu}_i^O = \bar{\mu}_i^O|_{x=L} - \bar{\mu}_i^O|_{x=0} \quad \text{for } i = v, e. \quad (3)$$

Here, $x = L$ is the location of the interface between the oxide and metal phases, and $x = 0$ is at the gas-oxide interface as shown in Fig. 1. Then, Eq. (1) becomes

$$\mathbf{J}_i = -M_i \Delta \bar{\mu}_i^O / L \quad \text{for } i = v, e. \quad (4)$$

The value of the electrochemical potential, $\bar{\mu}_i^O|_{x=0}$ in Eq. (3), at the oxide surface is given by the oxygen reduction reaction. The flux of vacancies at the gas-oxide interface is

$$\mathbf{J}_v = \kappa \prod_{g/o}, \quad (5)$$

where κ is the reaction rate constant at the gas-oxide interface and $\prod_{g/o}$ is the driving force for the reaction at the gas-oxide interface,

$$\prod_{g/o} = -\bar{\mu}_v^O|_{x=0} - \bar{\mu}_e^O|_{x=0} - \mu_g, \quad (6)$$

where μ_g is the chemical potential of oxygen in the gas and $\bar{\mu}_v^O|_{x=0}$ and $\bar{\mu}_e^O|_{x=0}$ are the vacancy and electron

electrochemical potentials at the gas-oxide interface, $x = 0$, in Fig. 1. As κ goes to infinity (very fast reactions), $\prod_{g/o}$ becomes very small (i.e., $\ll 1$). In other words, the flux is held finite while letting the reaction rate constant go to infinity. Thus, in the fast-reaction rate limit, local equilibrium is obtained,

$$\bar{\mu}_v^O|_{x=0} + \bar{\mu}_e^O|_{x=0} = -\mu_g. \quad (7)$$

This gives one equation in the two unknown concentrations, c_v and c_e , the defect concentrations of vacancies and electrons at the oxide surface, respectively. They are related to the chemical potentials of each species, μ_v and μ_e , given the value of the electrostatic potential at the oxide surface. In our case, we represent the chemical potentials in a Taylor's series expanded to first order [26],

$$\mu_i^O = \frac{\partial G^O}{\partial c_i} = \mu_{i,eq}^O + B_i^O (c_i^O - c_{eq}^O) \quad \text{for } i = v, e, \quad (8)$$

where c_i^O are defect concentrations of vacancies and electrons in the oxide and metal phases. The c_{eq}^O is the equilibrium defect concentrations (e.g., 10^{-3}) of the pure phases. The $\mu_{i,eq}^O$ is equilibrium chemical potential of the defects in the oxide phase that is a function of standard state chemical potentials and equilibrium defect concentrations [26]. The constants B_i^O are the second derivatives of the ideal solution model for the Gibbs free energy densities of the oxide at equilibrium [26]. Since the oxide surface is charged during the oxidation process, this provides a second equation for the concentrations of vacancies and electrons, c_v and c_e , at the oxide surface. The charge density ρ is given by the difference in the charged defect concentrations,

$$\rho^s = (c_v^O - c_e^O)F. \quad (9)$$

Here, F is the Faraday constant. Once ρ^s is fixed in Eq. (9), using Eq. (8) in Eq. (7) we set the concentrations of vacancies and electrons at the surface. Thus, when there is no charge at the surface c_v^O is equal to c_e^O , and $\Delta \mu_v^O$ and $\Delta \mu_e^O$ are identical. Oxygen reduction on the oxide surface is not considered in the classical Wagner theory, and thus to make connection with this treatment we set c_v^O equal to c_e^O .

The quasistationary approximation leads coupled currents in the absence of a magnetic field. Since there is no net current across the oxide layer [35,36], the local charge continuity equation from Eq. (2) is

$$\sum_{i=v,e} q_i \frac{\partial c_i}{\partial t} = -\nabla \cdot (\mathbf{J}_v - \mathbf{J}_e) = 0. \quad (10)$$

When the space charge does not change with time in the quasistationary limit, the coupled currents condition, $\mathbf{J}_v = \mathbf{J}_e$ in Eq. (1) holds at all the positions in bulk oxide during oxidation, regardless of oxide film thickness. Specifically,

$$\begin{aligned} \mathbf{J}_v = \mathbf{J}_e &= -M_v \Delta \bar{\mu}_v^O = -M_e \Delta \bar{\mu}_e^O = M_v \Delta (\mu_v^O + q_v F \psi^O) \\ &= M_e \Delta (\mu_e^O + q_e F \psi^O), \end{aligned} \quad (11)$$

where $\Delta \mu_v^O$ and $\Delta \mu_e^O$ are the constant chemical potential differences between the gas-oxide and oxide-metal interfaces during diffusion-limited growth. If M_v is not equal to M_e (e.g.,

$M_e = \alpha M_v$) in Eq. (11), Eq. (11) becomes

$$(1 - \alpha)\Delta\mu_e^O = (1 + \alpha)q_e F \Delta\psi^O, \quad (12)$$

where $\Delta\mu_e^O$ is a constant between the gas-oxide and oxide-metal interfaces during diffusion-limited growth. Thus, the electrostatic potential difference through the oxide, $\Delta\psi^O$, varies depending on a ratio of M_v and M_e . The local electrostatic potential is given by Gauss's law,

$$\nabla \cdot [\varepsilon^O \nabla \psi^O] = -\rho. \quad (13)$$

Here, ε^O is the permittivity of oxide film. In the thick film limit where charge neutrality holds, ψ^O is either a constant or is linear in one dimension. Therefore, the gradient of the electrostatic potential through the oxide increases with increasing the ratio of M_v to M_e , α , in Eq. (12).

To determine the velocity of the oxide-metal interface in the thick film limit, the electrochemical potential difference between the gas-oxide and oxide-metal interfaces is constant. Thus, from Eq. (4), the velocity v of the oxide-metal interface is

$$\frac{dL}{dt} = v = -\frac{1}{C} \mathbf{J}_i \cdot \hat{x} = \frac{M_i \Delta \bar{\mu}_i^O}{C} \frac{1}{L} \quad \text{for } i = v, e, \quad (14)$$

where C is the molar density of the oxide phase. This implies that the film thickness grows as $t^{1/2}$, assuming that the electrochemical potential differences are independent of film thickness. From Eq. (4), the parabolic rate constant k_p is given by

$$k_p = \frac{2M_i \Delta \bar{\mu}_i^O}{C}, \quad (15)$$

where $\Delta \bar{\mu}_i^O$ is given in Eq. (3). The thickness-independent rate constant in Eq. (15) gives a parabolic growth law.

B. Phase-field model

1. Model development

Sherman and Voorhees [26] developed a phase-field model describing an oxide film on a metal. We employ this model to study the evolution of oxide films in this work. The total free energy of the oxide-metal system [26] is

$$\mathcal{F}(\phi, c_v, c_e, \psi) = \int \left[G^\phi + G^{\text{tot}} + \frac{1}{2} \psi \rho \right] dV, \quad (16)$$

where ϕ is a phase-field variable, c_v and c_e are defect concentrations of vacancies and electrons, ψ is the electrostatic potential, and ρ is charge density. The phase-field variable ranges from 0 to 1, where $\phi = 0$ is the oxide phase and $\phi = 1$ is the metal phase. The phase-field free energy G^ϕ consists of a symmetric double well potential and a gradient energy penalty.

$$G^\phi = \frac{\epsilon}{2} |\nabla \phi|^2 + A \phi^2 [1 - \phi]^2. \quad (17)$$

As a result of Eq. (17), the equilibrium thickness and energy of the oxide-metal interface are ζ and γ_ϕ , given by

$$\zeta = \sqrt{\frac{2\epsilon}{A}} \quad \text{and} \quad \gamma_\phi = \frac{\sqrt{\epsilon A}}{3\sqrt{2}}. \quad (18)$$

Here, ϵ and A are the gradient energy coefficient and the height of the double well, respectively. In Eq. (16), the second term, G^{tot} , is an interpolation of the chemical free energy densities of the oxide and metal phases, G^O and G^M , [26] defined as

$$G^{\text{tot}} = p(\phi)G^M + [1 - p(\phi)]G^O, \quad (19)$$

where $p(\phi)$ is a common interpolation function,

$$p(\phi) = \phi^3 (10 - 15\phi + 6\phi^2). \quad (20)$$

The free energies of oxide and metal phases, G^O and G^M , are

$$G^O = \sum_{i=v,e} \left[\mu_{i,eq}^O(O) + \frac{1}{2} B_i^O (c_i^O - c_{eq}^O)^2 \right], \quad (21)$$

$$G^M = \sum_{i=v,e} \left[\mu_{i,eq}^M (c_i^M - c_{eq}^M) + \frac{1}{2} B_i^M (c_i^M - c_{eq}^M)^2 \right] + \Delta G^o, \quad (22)$$

where $c_i^O, c_{eq}^O, \mu_{i,eq}^O, B_i^O$ are defined in Eq. (8) in Sec. II A, and $c_i^M, c_{eq}^M, \mu_{i,eq}^M$ are the molar density of vacancy or electron, the equilibrium concentrations of vacancy or electrons, and the equilibrium chemical potential of the defects in the metal phase [26]. B_i^M is the second derivatives of the equilibrium Gibbs free energy densities of vacancy or electron in the metal, assuming an ideal solution [26]. ΔG^o is the difference in the equilibrium Gibbs free energy densities between the two phases evaluated at $c_i^O = c_{eq}^O$ and $c_i^M = c_{eq}^M$, again assuming the ideal solution for the Gibbs free energy densities [26]. Since we are assuming parabolic free energy functions, the derivative of the Gibbs free energy with respect to concentration does not diverge at zero or 1. Thus, when the driving force for oxidation is too high the concentrations can become less than zero or greater than 1, and the model is limited to small driving forces. In order to express G^{tot} in Eq. (16) in terms of defect concentrations (c_v, c_e), we use the average molar density, c_i and the interpolation function [26],

$$c_i = p(\phi)c_i^M + [1 - p(\phi)]c_i^O. \quad (23)$$

Using Eqs. (21)–(23), Eq. (19) becomes [26],

$$G^{\text{tot}} = \sum_{i=v,e} \left[\mu_{i,eq} (c_i - c_{eq}) + \frac{1}{2} \frac{B_i^O B_i^M}{B_i} (c_i - c_{eq})^2 + \frac{F^2 p(\phi)[1 - p(\phi)]}{2 B_i} (\Delta\psi^O)^2 \right] + p(\phi)\Delta G^o, \quad (24)$$

where c_{eq} is the average equilibrium defect density of the two-phase mixture,

$$c_{eq} = p(\phi)c_{eq}^M + [1 - p(\phi)]c_{eq}^O. \quad (25)$$

The interpolated equilibrium chemical potentials $\mu_{i,eq}$ and free energy coefficients B_i are

$$\mu_{i,eq} = \frac{p(\phi)B_i^O \mu_{i,eq}^M + [1 - p(\phi)]B_i^M \mu_{i,eq}^O}{B_i}, \quad (26)$$

$$B_i = p(\phi)B_i^M + [1 - p(\phi)]B_i^O. \quad (27)$$

The term $\Delta\psi^o$ in Eq. (24) is the Galvani potential between the bulk phases due to the difference in equilibrium chemical

potentials of the charged species. The Galvani potential is

$$\Delta\psi^o = \psi_{eq}^M - \psi_{eq}^O = \frac{\mu_{i,eq}^O - \mu_{i,eq}^M}{q_i F} \quad \text{for } i = v, e, \quad (28)$$

where the Galvani potential is $\psi_{eq}^M - \psi_{eq}^O$ or the difference of electrostatic potential between the oxide and metal phases at equilibrium. In Eq. (16), the third term, $\frac{1}{2}\psi\rho$, is the electrostatic energy density. The term ρ is charge density; it can be defined in terms of the difference in the charged defect concentrations. The potential is determined using Gauss's law, Eq. (13). However, ε^O is replaced by an interpolation of the oxide and metal permittivities,

$$\varepsilon(\phi) = p(\phi)\varepsilon^M + [1 - p(\phi)]\varepsilon^O, \quad (29)$$

where ε^O and ε^M are the permittivities of the oxide and metal phases, and the potential varies continuously from the oxide to metal.

To ensure that Gauss's law holds at all points, we add Gauss's law as a constraint and define a new energy \mathcal{L} [20,21,26] as

$$\mathcal{L} = \mathcal{F} - \int \lambda(\nabla \cdot [\varepsilon \nabla \psi] + \rho) dV, \quad (30)$$

where λ is a Lagrange multiplier, which is equal to $-\frac{1}{2}\psi$ in order to ensure that the variation of \mathcal{L} with respect to the nonconserved electrostatic potential is zero [26]. Using this result, the evolution equations for the phase-field variable and defect densities are [17,18,20,26,37,38]

$$\begin{aligned} \frac{\partial \phi}{\partial t} &= -M_\phi \frac{\delta \mathcal{L}}{\delta \phi}, \\ \frac{\delta \mathcal{L}}{\delta \phi} &= \left[2A\phi(-2\phi^2 + 3\phi - 1) + \varepsilon \nabla^2 \phi - \frac{\partial p(\phi)}{\partial \phi} \left(\Delta G^o + \sum_{i=v,e} \left\{ -\mu_{i,eq} (c_{eq}^M - c_{eq}^O) \right. \right. \right. \\ &\quad \left. \left. \left. + \frac{B_i^O B_i^M}{B_i} \left[\frac{(B_i^M - B_i^O)}{2B_i} (c_{eq}^M - c_{eq}^O) - \frac{1}{B_i} q_i C \Delta \psi^o - (c_{eq}^M - c_{eq}^O) \right] (c_i - c_{eq}) \right. \right. \right. \\ &\quad \left. \left. \left. + \frac{C^2}{2} (\Delta \psi^o)^2 \frac{[1 - p(\phi)]^2 B_i^M - p(\phi)^2 B_i^O}{(B_i)^2} \right\} \right) - \frac{1}{2} \frac{\partial \varepsilon}{\partial \phi} |\nabla \psi|^2 \right], \end{aligned} \quad (31)$$

$$\frac{\partial c_i}{\partial t} = \nabla \cdot \left[M_i(c_i) \nabla \frac{\delta \mathcal{L}}{\delta c_i} \right] = \nabla \cdot M_i(c_i) \nabla \left[\mu_{i,eq} + \frac{B_i^O B_i^M}{B_i} (c_i - c_{eq}) \pm C\psi \right] \quad \text{for } i = v, e, \quad (32)$$

where $M_v(c_v)$ and $M_e(c_e)$ are the defect mobilities of vacancies and electrons, and M_ϕ is the phase-field mobility. The evolution equations are nondimensionalized as in [26]

$$\begin{aligned} \tilde{x} &= \frac{x}{L_D}, \quad \tilde{c} = \frac{c}{C}, \quad \tilde{t} = \frac{t D_0}{L_D^2}, \quad \tilde{G} = \frac{G L_D^3}{k_B T}, \\ \tilde{\varepsilon} &= \frac{\varepsilon L_D}{k_B T}, \quad \tilde{\varepsilon} = \frac{\varepsilon R T L_D N_A}{F^2}, \quad \tilde{\rho} = \frac{\rho L_D^3 N_A}{F}, \\ \tilde{\mu} &= \frac{\mu C L_D^3}{k_B T}, \quad \tilde{\psi} = \frac{\psi F}{R T}, \quad \tilde{C} = C L_D^3 N_A, \\ \tilde{M}_i &= \frac{\tilde{M}_i k_B T}{D_0 C^2 L_D^3}, \quad \tilde{M}_\phi = \frac{M_\phi k_B T}{D_0 L_D}, \end{aligned} \quad (33)$$

where $M_i(c_i) = \tilde{M}_i c_i$. The values of dimensional parameters in Eq. (33) are listed in Table I.

A computational challenge is the rapid change in the defect concentration at the interface that is required to capture the electrostatic double layers at the interface. Sherman and Voorhees [26] relaxed the electron screening length (L_S) in the metal to make the computation feasible and showed that the defect structure and electrostatic potential profiles in the oxide are unaffected. Thus, we chose the relaxation factor, L_S/L_D , of 0.5 in this work. The oxygen vacancy normally carries an effective charge of +2. But we assume +1 for the oxygen vacancy charge in a modeling perspective. This is because the effective charge of +2 just gives a factor of 2 in the evolution equations when we assume a charge neutrality in the bulk

phases. Previously, the phase-field equations given in Eq. (31) and (32) were solved with an explicit Euler scheme using second-order finite differences on a uniform grid [26]. In order to greatly reduce the computational cost of solving these equations that stem from the rapidly changing electrostatic double layers, we use the open source Multiphysics Object-Oriented Simulation Environment (MOOSE) [39] developed in Idaho National Laboratory (INL). MOOSE is a massively parallel finite element-based system designed to solve large systems of equations using the Jacobian-free Newton-Krylov (JFNK) method and implicit time integration schemes. Furthermore, MOOSE is based on the modular free energy approach with automatic differentiation [40], which simplifies and accelerates the development of new multiphase-field models. For

TABLE I. Representative parameters used in this simulation. The values are from [26].

C	$9 \times 10^4 \text{ mol/m}^3$	ε^O	$70\varepsilon_0$
c_{eq}^O	0.001	ε^M	ε_0
c_{eq}^M	0.999	ΔG^o	$6.311 \times 10^{10} \text{ J/m}^3$
T	1000 K	$\Delta \psi^o$	0.05 V
L_D	$5.5485 \times 10^{-9} \text{ m}$	γ_ϕ	$2 \times 10^{-3} \text{ J/m}^2$
D_0	$10^{-13} \text{ m}^2/\text{s}$	ζ	$0.1 L_D$
M	$2.2574 \times 10^{-16} \text{ mol}^2/\text{J s m}$		

the two-dimensional simulations, we use mesh adaptivity for computational feasibility as shown below.

In order to solve the second-order differential equation for the electrostatic potential given in Eq. (13) coupled with the evolution equations in Eq. (31) and (32), we need two boundary conditions as described in Sec. II A. First, we set the time-independent value of electrochemical potentials, $\bar{\mu}_v$ and $\bar{\mu}_e$ at the gas-oxide interface, to a value at the solid-gas interface less than that in equilibrium. This is based on the two assumptions that local equilibrium is present at the gas-oxide interface, see Eq. (7), and that there is a constant charge density at the gas-oxide interface; see Eq. (9). The absolute value of the potential is arbitrary, so the value of the electrostatic potential is chosen to be zero at the gas-oxide interface. The other boundary condition is that a gradient of electrochemical potentials, $\nabla\bar{\mu}_v$ and $\nabla\bar{\mu}_e$, of vacancy and electron is equal to zero at the far end of the domain in the metal, $x = M$, shown in Fig. 1, which is chosen sufficiently far from the metal-oxide interface that the width of the metal does not affect the results.

The total change in the volume V^O of the oxide is

$$\frac{dV^O}{dt} = -A \int \frac{\partial p(\phi)}{\partial t} dV = -A \int \frac{\partial p(\phi)}{\partial \phi} \frac{\partial \phi}{\partial t} dV, \quad (34)$$

where A represents a cross-sectional area. The interpolation function $p(\phi)$ is also the local volume fraction of the metal phase in the oxide-metal system. Therefore, the one-dimensional velocity v of the oxide-metal interface is

$$v = \frac{\partial V^O}{\partial t} \frac{1}{A} = - \int \frac{\partial p(\phi)}{\partial \phi} \frac{\partial \phi}{\partial t} dx. \quad (35)$$

2. Transport kinetics

The flux of species (i) in the phase-field model is

$$\mathbf{J}_i = -M_i(c_i) \nabla \frac{\delta \mathcal{L}}{\delta c_i} \quad \text{for } i = v, e, \quad (36)$$

where \mathcal{L} , M , and J_i are a Lagrangian, mobility, and diffusion flux, respectively. The flux in the phase-field model far from the interfaces becomes

$$\begin{aligned} \mathbf{J}_i &= -M_i(c_i) \nabla \frac{\delta \mathcal{L}}{\delta c_i} \\ &= -M_i(c_i) \nabla [\mu_{i,eq}^O + B_i^O(c_i - c_{eq}^O) + q_i F \psi] \\ &= -M_i(c_i) [B_i^O \nabla c_i + q_i F \nabla \psi] \\ &= -M_i(c_i) \left[\frac{RTC}{c_{eq}^O(C - c_{eq}^O)} \nabla c_i + q_i F \nabla \psi \right] \quad \text{for } i = v, e, \end{aligned} \quad (37)$$

where B_i^O are the second derivatives of the free energy densities at equilibrium. From the zero gradient boundary condition of electrochemical potentials at the metal edge, the interface motion is only driven by the flux from the gas-oxide interface. This gives no net currents in the oxide film. In other words, the total charge flux is zero in a system. The mole fraction of defects in the oxide is much less than 1 in this work; then

$$\frac{RTC}{c_{eq}^O(C - c_{eq}^O)} \simeq \frac{RT}{c_{eq}^O/C}. \quad (38)$$

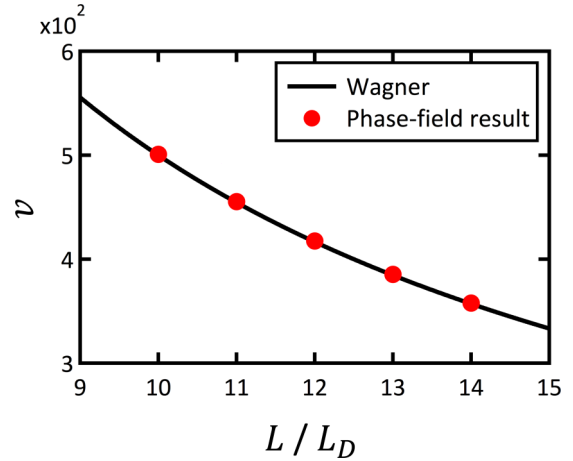


FIG. 2. Oxidation velocity by Eq. (35) as a function of oxide thickness L . The black line indicates the Wagner theory parabolic growth law in Eq. (14).

III. RESULTS AND DISCUSSIONS

A. Thick film limit

We first verified that the phase-field model recovers the Wagner parabolic rate law in the thick film limit with zero surface charge density in Eq. (9) at the gas-oxide interface to be consistent with the assumptions made by Wagner. In addition, we also take $M_i(c_i) = \bar{M}_i$, a constant mobility, see below where this assumption is relaxed. The oxide thickness is ten times larger than the Debye length L_D , which leads to a film that is largely charge neutral, except for the double layers at the interfaces. According to Wagner's theory, a parabolic rate law is obtained if the species move in one dimension due to a fixed chemical potential difference between the two surfaces and the oxide-metal interface [6]. As mentioned above, in order to induce a nonzero flux at the gas-oxide interface, the electrochemical potentials at the gas-oxide interface are chosen to be less than the electrochemical potentials in equilibrium. For simplicity, mobilities of vacancy and electron, $\bar{M}_v = \bar{M}_e$, are chosen to be identical in Eq. (32). If \bar{M}_v and \bar{M}_e are not equal, this induces a gradient of electrostatic potential through the oxide since there is no net current flowing through the oxide, as discussed in Sec. II A. Figure 2 shows the velocity of the oxide-metal interface that is growing into the metal phase as a function of oxide thickness. The phase-field approach using high mobility recovers a parabolic growth law in Eq. (14).

In contrast to the analytical model discussed above, where the results are compared to the Wagner model, Figs. 3(a) and 3(b) show the case where there is a nonzero surface charge density at the gas-oxide interface, see Eq. (9), due to surface oxygen reduction. The shift in the electrostatic and electrochemical potentials due to a nonzero charge density at gas-oxide interface does not influence the evolution equations given in Eq. (31) and (32) because only a difference or gradient in these quantities between the oxide and metal phases is important. Figures 3(a) and 3(b) show that the electrochemical potentials $\bar{\mu}_i$ of anion vacancies v and electrons e across the oxide-metal interface depends on the order-parameter mobility \bar{M}_ϕ in the thick film limit where

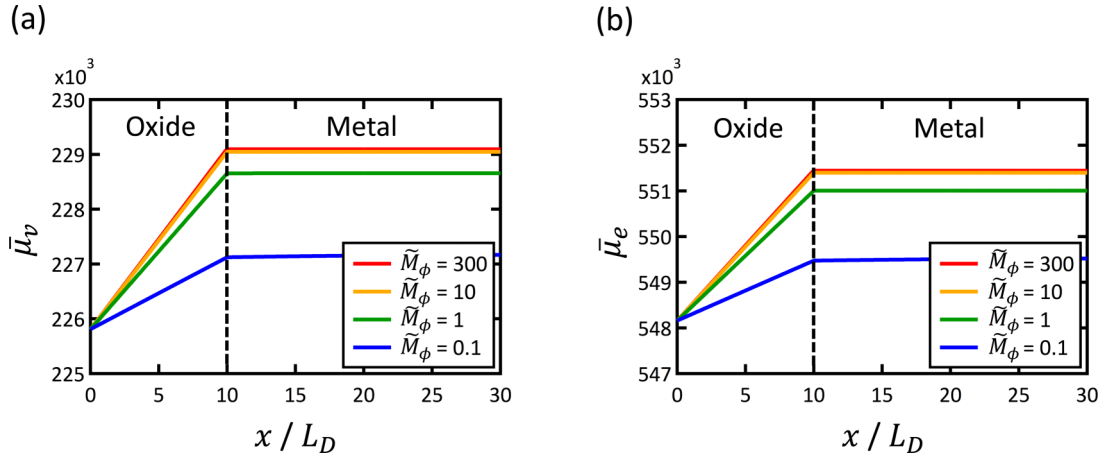


FIG. 3. The nondimensional electrochemical potential, $\bar{\mu}_i$, profiles across the oxide-metal interface as a function of order-parameter mobility, $\tilde{M}_\phi = 300, 10, 1, 0.1$, in Eq. (31). The charged species i are (a) vacancies v , and (b) electrons e , respectively. The oxide thickness is chosen as ten times larger than the Debye length L_D , which results in charge neutrality throughout the oxide layer. The dotted line represents the location of the interface between the oxide and metal phases where the order parameter ϕ is equal to 0.5.

charge neutrality in the bulk holds. The interface is in local equilibrium when the mobility is high (e.g., $\tilde{M}_\phi = 300$) in Figs. 3(a) and 3(b). Local equilibrium does not hold at the interface when the oxide-metal interface becomes reaction limited as the mobility decreases, such as for the case when $\tilde{M}_\phi = 0.1$. The electrochemical potentials of the vacancies or electrons at the oxide-metal interface are not equal to their equilibrium values since the nonzero surface charge density at the gas-oxide interface increases electrochemical potential in the oxide phase.

Figure 4(a) shows concentration profiles of the anion vacancies and electrons relative to equilibrium concentrations c_{eq} for two different cases, $\tilde{M}_\phi = 300$ and 0.1, where c_{eq} is $p(\phi)c_{eq}^M + [1 - p(\phi)]c_{eq}^O$. The values of c_{eq}^M and c_{eq}^O are shown in Table I. Figures 4(b) and 4(c) show the charge density, ρ , and the electrostatic potential, ψ , profiles near the oxide-metal interface with oxide thickness $L = 10L_D$. Since the film is charge neutral far from the interfaces, Laplace's equation for electrostatic potential holds in Eq. (31), and thus there is a constant electrostatic potential through the bulk oxide phase, as shown in Fig. 4(c). As a result of the Gibbs free energy densities being given by a quadratic function of concentration, see Eqs. (22) and (23), the chemical potential gradient is linear with respect to the concentration difference, $c_i - c_{eq}$, through the oxide phase. Therefore, the concentration profiles for the vacancies and electrons in the bulk phases are linear away from the interface; see Fig. 4(a). The charge is positive on the metal side of the interface due to a deficit of electrons, and negative on the oxide side, caused by excess electrons in Fig. 4(b). Since local equilibrium holds at the oxide-metal interface, when the mobility is high during the diffusion-limited growth, the electrostatic potential difference between the bulk oxide and bulk metal is equal to the equilibrium Galvani potential difference $\Delta\psi^o$ in Table I; see $\tilde{M}_\phi = 300$ in Fig. 4(c). The nonzero gradient in the potential at the gas-oxide interface is due to surface charging as a result of the oxygen reduction. When the growth of the oxide is controlled by the reaction at the interface, an electrostatic overpotential η develops across the interface; see Fig. 4(c). Thus, the value

of the electrochemical potential at the interface, shown in Figs. 3(a) and 3(b), decreases since there is now a driving force needed to move vacancies or electrons across the oxide-metal interface. The shift in the electrochemical potential of a vacancy through the metal in Fig. 3(a) is due to the shift in concentrations in bulk metal shown in Fig. 4(a) and is balanced by the electrostatic overpotential. However, most of the shift in the electrochemical potential of electrons in the metal seen in Fig. 3(b) is due to the change in the electrostatic potential, not the concentrations of defects. The oxidation velocity into the metal phase as a function of oxide thickness is shown in Fig. 4(d). There is a clear transition in the growth law from parabolic to linear as the interfacial mobility decreases. Since the diffusion field is relaxed on the timescale of interface motion, the electrochemical potentials are well described by linear functions of position, as discussed in Sec. II A. Since the charging that results from oxygen reduction shifts the overall electrostatic potential profile upward, the rate constant a in the parabolic growth law differs from the rate constant found when there is no charging at that surface. From the results in Figs. 4(a)–4(c), we find that the oxide will grow linearly in time when the oxidation reaction is controlled by the reaction at the oxide-metal interface.

Figures 5(a) and 5(b) show the charge density and electrostatic potential across the oxide-metal interface when mobility of the interface is small, $\tilde{M}_\phi = 0.1$. In this limit, the reaction rate at the metal-oxide interface is important and the phase-field model predicts an overpotential at the interface. Furthermore, as shown in Fig. 5(c) this overpotential varies linearly with interfacial velocity. Thus, the phase-field model recovers the classical Butler-Volmer result for electrode kinetics where the current density (flux) is linearly proportional to the electrostatic overpotential in the low overpotential region. Butler-Volmer kinetics therefore arises naturally from the phase-field model since the electrostatics in the interface region are determined self-consistently, similar to that found by Guyer *et al.* [21] in their phase-field model of an electrode-electrolyte system.

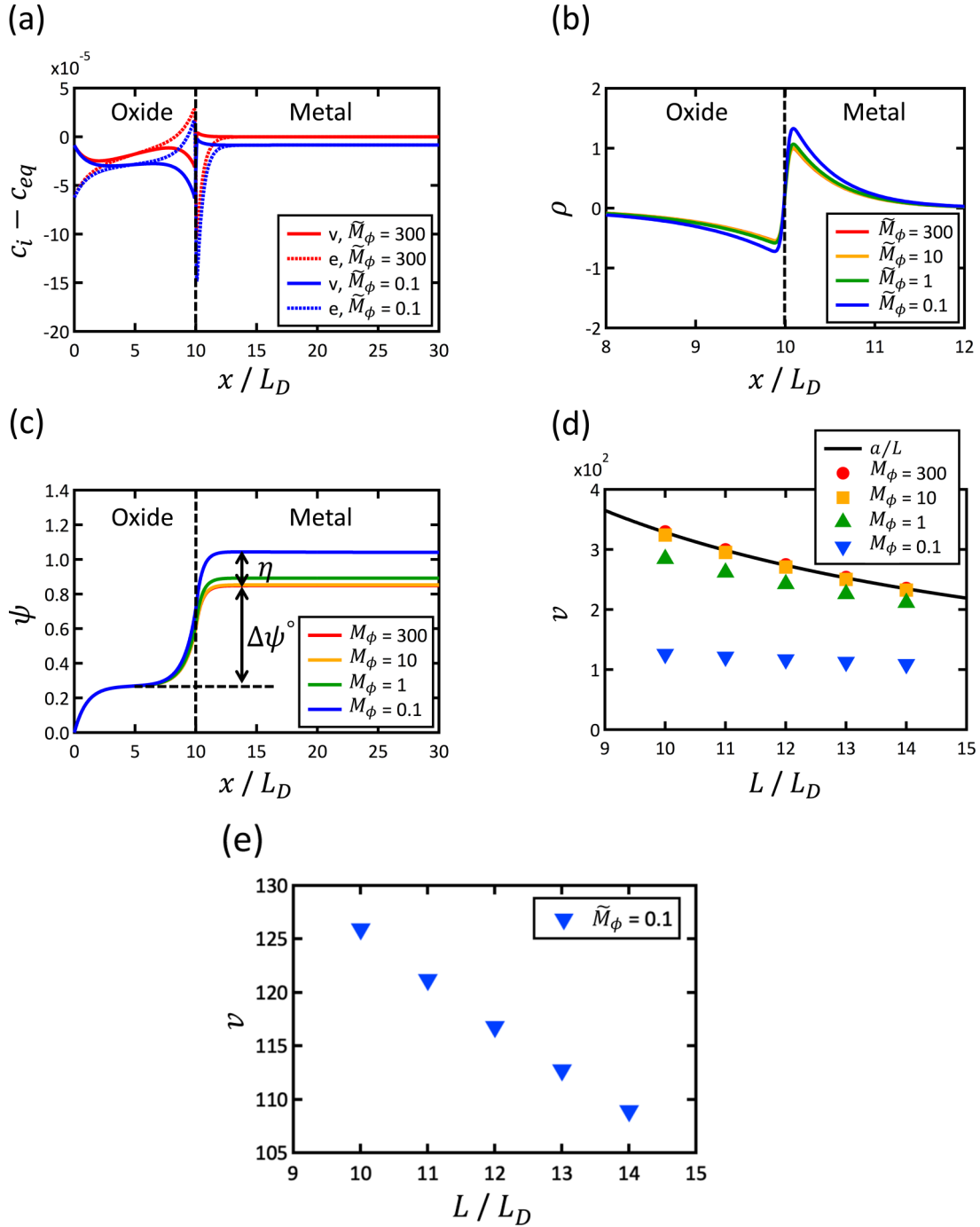


FIG. 4. (a) Concentration profiles of vacancies c_v and electron c_e relative to equilibrium concentrations c_{eq} , for two different order-parameter mobilities, $\tilde{M}_\phi = 300, 0.1$, in Eq. (31) in the thick film limit. The term c_{eq} is equal to $p(\phi)c_{eq}^M + [1 - p(\phi)]c_{eq}^O$ where $p(\phi)$ is an interpolation function as described in Eq. (20). The values of c_{eq}^M and c_{eq}^O are shown in Table I. (b) Charge density, ρ , and (c) electrostatic potential, ψ , profiles across the oxide-metal interface with order-parameter mobilities, $\tilde{M}_\phi = 300, 10, 1$, and 0.1 , in Eq. (31). The term $\Delta\psi^0$ represents the Galvani potential between the two bulk phases in equilibrium. The term η is the electrostatic overpotential across the interface. The dotted lines represent the location of the interface between the oxide and metal phases where ϕ is equal to 0.5 . (d) Oxidation velocity given by Eq. (35) as a function of oxide thickness L divided by Debye length L_D . The black line indicates a constant, a , divided by L/L_D and that is given by a classical Wagner-type rate law in Eq. (14). (e) Oxidation velocity with order-parameter mobility of 0.1 on a magnified scale in (d). It is evident that the velocity is not constant, but changes by 15% with distance between 10 and $14L_D$.

B. Thin film limit

In this section, we investigate the kinetics of oxidation in the thin film limit where charge neutrality is not satisfied.

Figures 6(a) and 6(b) show the electrochemical potential profiles for an oxide-metal interface when the oxide thickness L is comparable to Debye length L_D . In the large mobility limit local electrochemical potential equilibrium holds at the

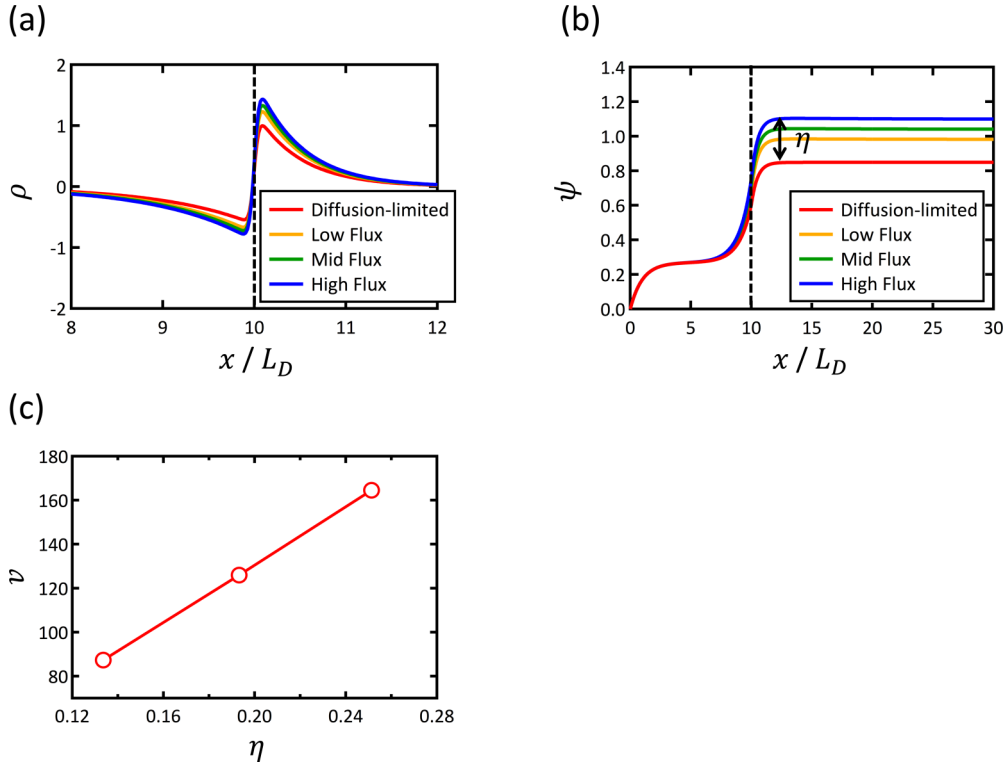


FIG. 5. (a) Charge density ρ and (b) electrostatic potential ψ across the oxide-metal interface with order-parameter mobilities, $\tilde{M}_\phi = 0.1$, in Eq. (31). (c) Growth rate v versus electrostatic overpotential η across the interface. The overpotential is linearly proportional to growth rate in the low overpotential region.

oxide-metal interface, similar to the thick film behavior. A comparison of Figs. 3 and 6 demonstrates that the electrochemical potentials at the interface deviate from their equilibrium values more significantly for the thin film compared to the thick film, as \tilde{M}_ϕ decreases from 300 to 0.1. The electrochemical potentials vary linearly in space even for thin films because the diffusion field is relaxed, and we have assumed that the mobility is independent of concentration.

Figure 7(a) shows the defect concentration profiles relative to the bulk equilibrium concentrations $c_i - c_{eq}$ for a growing

oxide in the thin film limit. The metal is more negatively charged than in the thick film limit due to the interaction between the double layers at the gas-oxide and oxide-metal interfaces [26]. The double layer becomes larger with decreasing \tilde{M}_ϕ , as shown in Fig. 7(b). Similarly to that found in the thick film limit as the oxidation reaction rate becomes governed by the reaction at the oxide-metal interface, or mobility of the oxide-metal interface, an overpotential develops across the interface as shown in Fig. 7(c). Figure 7(d) shows the oxide growth rate into the metal phase as a function of film

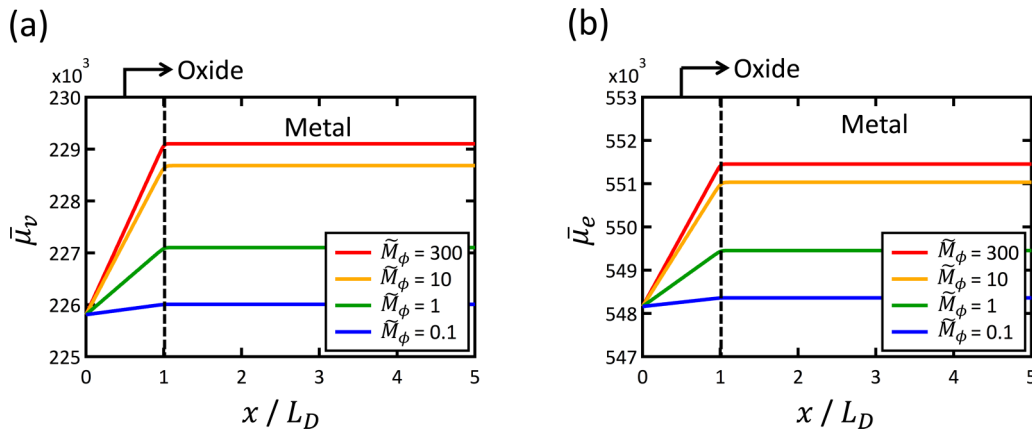


FIG. 6. The nondimensional electrochemical potential, $\bar{\mu}_i$, profiles across the oxide-metal interface as a function of order-parameter mobility, $\tilde{M}_\phi = 300, 10, 1, 0.1$, in Eq. (31). The charged species i are (a) vacancies v and (b) electrons e , respectively. The oxide thickness is comparable to the Debye length L_D in the thin film limit where charge neutrality does not hold. The dotted lines represent the location of the interface between the oxide and metal phase where the order parameter ϕ is equal to 0.5.

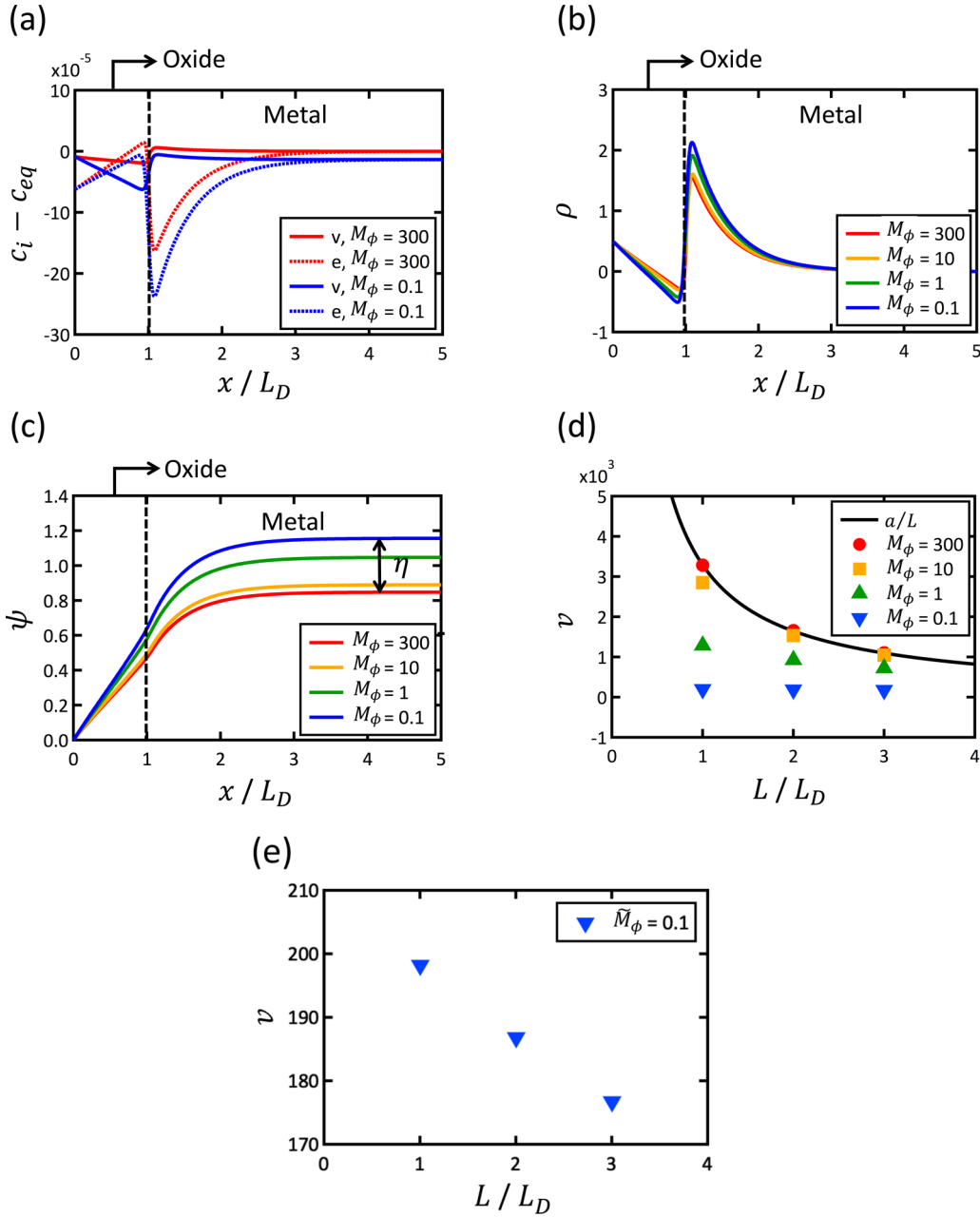


FIG. 7. (a) Concentration profiles of vacancies c_v and electrons c_e relative to c_{eq} for two different order-parameter mobilities, $\tilde{M}_\phi = 300$ and 0.1, in the thin film limit. The term c_{eq} is equal to $p(\phi)c_{eq}^M + [1 - p(\phi)]c_{eq}^O$ where $p(\phi)$ is an interpolation function as described in Eq. (20). (b) Charge density, ρ , and (c) electrostatic potential, ψ , profiles across the oxide-metal interface with order-parameter mobilities, $\tilde{M}_\phi = 300$, 10, 1, and 0.1, in Eq. (31). The term η is the electrostatic overpotential across the interface. The dotted lines represent the location of interface between the oxide and metal phases where ϕ is equal to 0.5. (d) Oxidation velocity given by Eq. (35) as a function of oxide thickness L divided by Debye length L_D . The black line indicates a constant a divided by L/L_D and refers to a Wagner-type rate law in Eq. (14). (e) The rescaled figure shows the oxidation velocity with an order-parameter mobility of 0.1 and shows that velocity changes by 11% with distance between 1 and $3L_D$.

thickness. It is clearly seen that the growth-law transitions from parabolic to linear as \tilde{M}_ϕ decrease. Comparing Figs. 4(d) and 7(d) implies that the growth-law transition occurs at higher values of \tilde{M}_ϕ in the thin film limit than in the thick film limit. Therefore, growth in the thin film limit will more likely follow a linear growth law where the interface motion is controlled by the oxidation reaction at the oxide-metal interface. This is because the growth rate is higher in the thin film limit

than in the thick film limit, leading to nonequilibrium even when using a small interfacial mobility. Our findings here are consistent with experimental observations of a transition from reaction- to diffusion-controlled growth during inward oxidation, such as during the growth of silicon oxide and chromium oxide [11,12].

In the high mobility limit where the interface is in local equilibrium, the growth rate of the film is diffusion controlled

yielding a parabolic growth law as shown Fig. 7(d), despite the fact that the film is charged. As we discussed in Sec. II A, when the mobility is independent of composition and the diffusion field governed by the quasistationary approximation, the electrochemical potentials must vary linearly with position. Thus, the spatial variations in the chemical potentials (or concentration) and electrostatic potential fields compensate each other to yield an electrochemical potential that varies linearly in space. Specifically, the two terms in the bracket in Eq. (37) compensate each other in our phase-field model. To gain further insight into the reasons for parabolic growth in the thin film limit, we examine the electrostatic potential difference between oxide surface and bulk metal,

$$\begin{aligned} q_i F \Delta \psi &= q_i F (\psi^M - \psi^O) \\ &= \mu_{i,eq}^O - \mu_{i,eq}^M + B_i^O (c_i^O - c_{eq}^O) \\ &\quad - B_i^M (c_i^M - c_{eq}^M) \quad \text{for } i = v, e. \end{aligned} \quad (39)$$

Here, c_i^M is equal to c_{eq}^M since the growth rate is diffusion limited. The concentrations of v and e at the gas-oxide interface are fixed due to a constant surface charge density and local equilibrium of electrochemical potentials with the gas phase. Thus, even in the thin film limit the electrostatic potential difference between the surface and metal is a constant during diffusion-limited oxide growth. The electrochemical potential difference between the oxide-metal interface and the surface is a constant during growth, thereby giving the Wagner-type parabolic growth law even in the thin film limit. In the thick film limit, the defect concentration and electrostatic potential decay exponentially as in Gouy-Chapman theory [26] on a length scale L_D . Thus, the defect concentrations, charge density, and electrostatic potential profiles are approximately linear in the thin film limit when there is a nonzero surface charge as shown in Figs. 7(a)–7(c).

The surface charging effect itself does not influence the overpotential at the interface given a constant electrochemical potential difference in the thin film limit. Specifically, the difference between $\bar{\mu}_v^O|_{x=0} + \bar{\mu}_e^O|_{x=0}$ and the gas chemical potential in equilibrium, $\mu_{g,eq}$, is a driving force for oxidation. When we assume a constant driving force of oxidation for given a value of μ_g , the values of the electrochemical potentials at the gas-oxide interface will vary with the surface charge density in Eq. (10). However, since the driving force of oxidation, $\mu_g - \mu_{g,eq}$, is a constant, the overpotential at the oxide-metal interface is only affected by its kinetics or the phase-field mobility. In the Supplemental Material [41], we see that the coupled current condition holds where $\mathbf{J}_v = \mathbf{J}_e$. Specifically, there is a nonzero slope of electrostatic potential in Figs S.1(e) and S.1(f) [41] when the mobilities of vacancy and electron are not equal; $\bar{M}_v = 0.6$, $\bar{M}_e = 3$. This gives differences in the electrochemical potential gradients of vacancies and electrons in Figs S.1(a)–S.1(d) in the thick and thin film limit. Based on this, our phase-field method can be easily written in terms of one defect variable and the coupled current condition, making it yet more computationally efficient.

The previous results assume that the mobility of vacancies and electrons is independent of concentration, $M_i(c_i) = \bar{M}_i$. This is used to assure that we recover the classical Wagner

treatment in the thick film zero-surface-charge limit. In the Wagner treatment [42], the rate constant in the parabolic growth law, a , is as a function of the spatially varying concentrations of cations and electrons. Wagner takes the integral of the product of these concentrations over the film thickness to be a constant, and thus obtains a thickness-independent rate constant. Thus, a time- (or thickness-) independent parabolic rate constant can be obtained in the phase-field model if we assume a concentration-independent mobility. Otherwise, the rate constant becomes time (or thickness) dependent because defect concentration at a certain point varies with time during growth in the phase-field model.

To examine the effects of this approximation, we compare the results where $M_i(c_i) = \bar{M}_i$ with those where mobility depends on concentration, $M_i(c_i) = \bar{M}_i c_i$. The factor of 10^2 is included due to low defect concentrations in oxide. Figures 8(a)–8(d) show the defect concentration and electrostatic potential profiles across the oxide-metal interface with or without the additional defect concentration term in the mobility. In the thick film limit in Figs. 8(a) and 8(b), the defect concentration and electrostatic potential profiles for both $M_i(c_i) = \bar{M}_i$ and $M_i(c_i) = 10^2 \bar{M}_i c_i$ are very similar. However, in the thin film limit, a concentration-dependent mobility leads to a small difference in the defect concentration and electrostatic potential profiles, as shown in Figs. 8(c) and 8(d). In particular, the vacancy concentration profile shown in Fig. 8(c) is now nonlinear, which gives a lower flux near the interface. This is illustrated in Fig. 8(e) which shows the diffusion flux, $|\mathbf{J}_i| = |M_i(c_i) \nabla \bar{\mu}_v|$, as a function of distance across the oxide-metal interface. This nonlinear defect concentration profile is due to a significant difference between the phase-field variable and defect mobility. This effect decreases as oxide film thickness increases due to slower growth kinetics of the oxide. The oxidation velocity as a function of oxide film thickness is shown in Fig. 8(f). The black line is a parabolic growth rate with a fixed rate constant. Clearly, the growth rate of the film where $M_i(c_i) = 10^2 \bar{M}_i c_i$ is not parabolic. To quantify this deviation from parabolic kinetics, the rate constant a is determined assuming a parabolic growth when the oxide film thickness is $10L_D$. We find that the rate constant is approximately 10% lower for films of thickness $1L_D$, and 4% lower for films of thickness $2L_D$. Thus, a concentration-dependent mobility leads to slightly nonparabolic growth and higher growth rates for small film thicknesses. The deviation from parabolic kinetics becomes smaller as the film thickness increases. Thus, for the parameters taken in the simulation, where there is a small defect flux and the equilibrium defect concentrations in oxide are on the same order of magnitude, a concentration-independent mobility assumption is a reasonable approximation.

To illustrate one of the major advantages of the phase-field method, we investigate the evolution of a nonplanar interface during oxide growth. In this case, we examine the evolution of a nonplanar oxide-metal interface where the amplitude of the nonplanar interfacial perturbation is comparable to the Debye length. The mobility of the oxide interface is large, and thus growth is diffusion limited and the mobilities of the vacancies and electrons are constants. It is also assumed that diffusion in the oxide dominates the growth process. Under these conditions, Bobeth *et al.* [2] predict that the oxide-metal

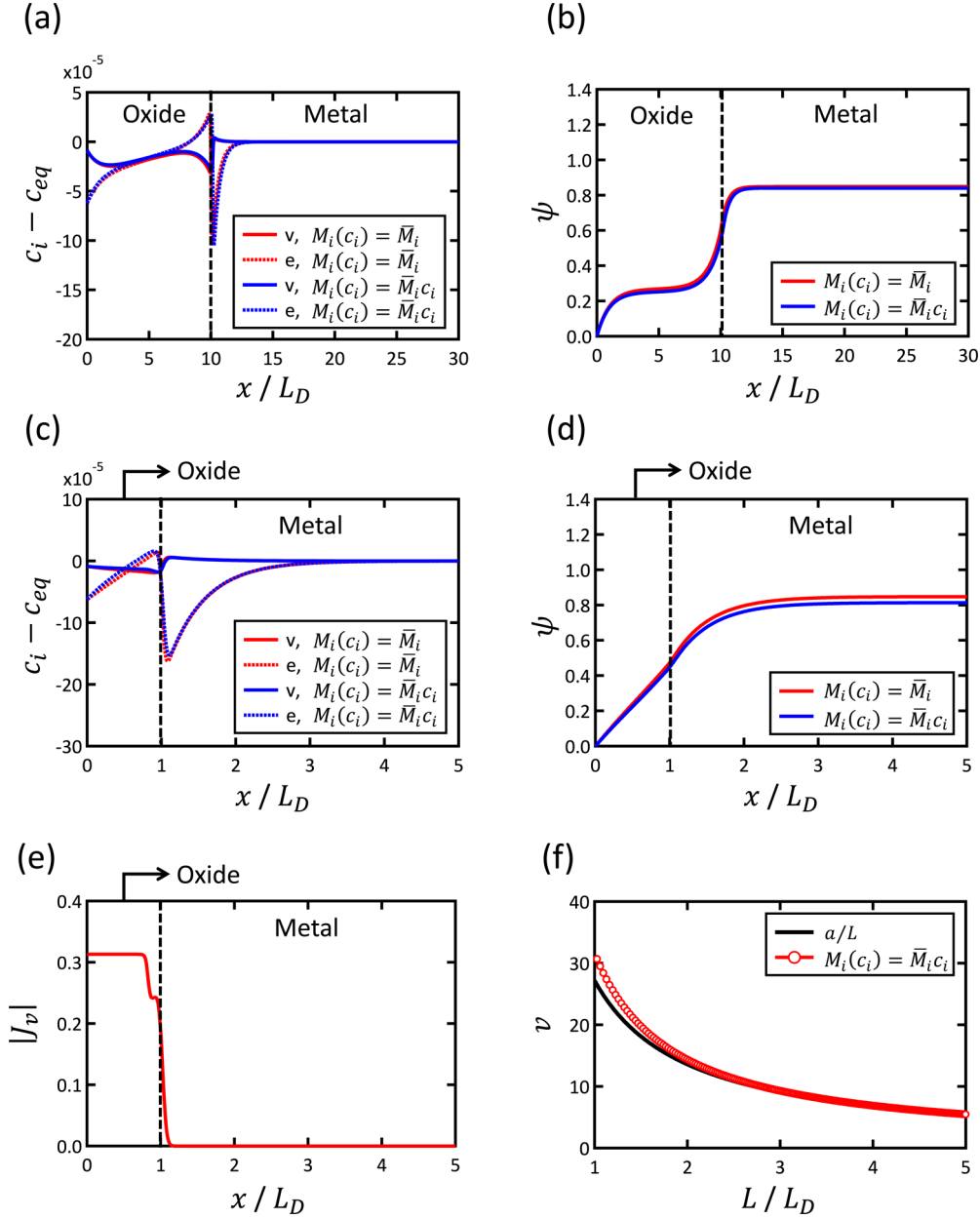


FIG. 8. Concentration profiles of vacancies c_v and electrons c_e relative to c_{eq} in the (a) thick and (c) thin film limit. Electrostatic potential, ψ , profiles across the oxide-metal interface in the (b) thick and (d) thin film limit. Red (and blue) curve represents phase-field model results without (and with) additional defect concentration, $M_i(c_i) = \bar{M}_i c_i$, in Eq. (32). (e) Diffusive flux of vacancy versus distance from $|\mathbf{J}_i| = |M_i(c_i) \nabla \mu_v|$ in the thin film limit. (f) Dimensionless oxidation velocity versus oxide film thickness. The black curve represents a parabolic growth rate with a fixed rate constant assumption. The rate constant a is taken from when oxide film thickness is $10L_D$. The phase-field model results and a parabolic growth law agree well when the film thickness is larger than $2L_D$, but diverge where film thickness becomes close to $1L_D$.

interface is morphologically stable. However, this prediction was made using linear stability theory, which is limited to small amplitude perturbations. We will use the phase-field model to investigate the case for large amplitude interfacial perturbations. Given the sharp transitions in electron, vacancy, and potential near the interfaces, along with the need to resolve the long-range diffusion fields, it was necessary to use the mesh adaptivity implemented in the open source Multiphysics Object-Oriented Simulation Environment (MOOSE) code [40] as shown in Fig 9(a). Figures 9(b)–9(d) show that the concentration and potential fields vary along the interface

as well as away from the interface. This spatial variation leads to an evolution of the nonplanar interface during oxide growth. There are lateral gradients in the defect concentrations, as shown in Figs. 9(c) and 9(d), unlike the one-dimensional model. Figure 10 shows the temporal evolution of the morphology of the interface when the oxide is growing into the metal, showing that the nonplanarity of the interface becomes smaller with time (see video in Supplemental Material [41]). The defect concentrations change rapidly at the interface due to the electrostatic double layer, and we find that the thickness of the double layer is not uniform along the interface.

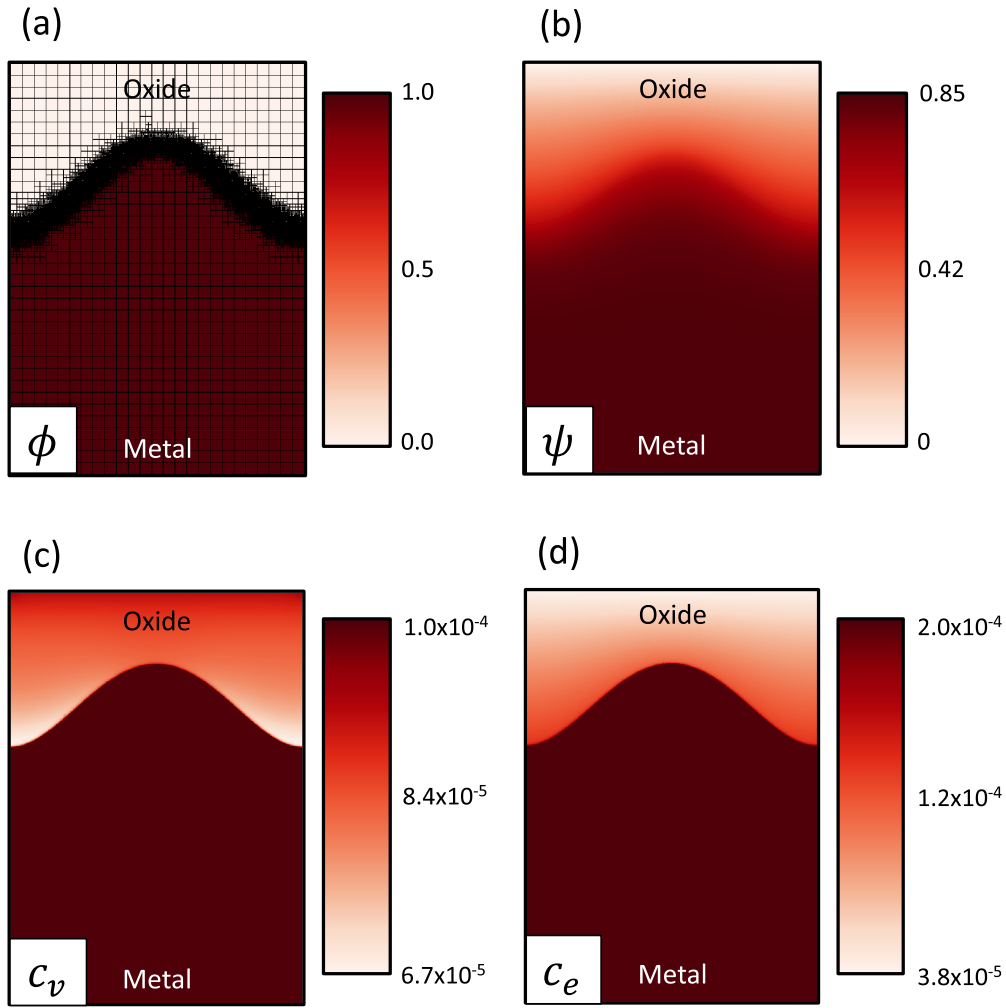


FIG. 9. (a) Phase-field variable, (b) electrostatic potential, (c) vacancy, and (d) electron defect concentrations across the oxide-metal interface in two dimensions, $5L_D$ by $7L_D$. For two-dimensional simulations, we used mesh adaptivity in the open source Multiphysics Object-Oriented Simulation Environment (MOOSE) for computational efficiency.

This phase-field simulation is consistent with experiment where the interface smoothing was observed during the inward growth of aluminum oxide [34]. In the future, we plan on including alloying effects or elastic stress to examine cases where the interface may be morphologically unstable [43,44].

To understand why the interfacial perturbation decays, Figs. 11(a)–11(d) give comparisons of the defect

concentrations, electrostatic potential, and electrochemical potentials across the oxide-metal interface between the flat and perturbed interfaces. Unlike one-dimensional models of oxidation, the gradient of the electrochemical potentials through oxide changes with position along the perturbed interface. Using Fig. 11(e) the mechanism for stabilization becomes clear. In this case, since a peak is closer to the oxide-vapor surface than for a planar interface, the gradient in the electrochemical potential is higher at a peak than at a planar interface, and this region of interface grows faster than a planar interface. By contrast, since the trough is farther from the oxide-vapor surface than a planar interface, the gradient in the electrochemical potential is lower than at a planar interface and thus the growth rate in this region is lower than that for a planar interface. As a result, the peaks grow faster than a planar interface while the troughs grow slower than a planar interface. Thus, the perturbations decay and a planar thin film results. The phase-field model includes interfacial energy, which is a well-known stabilization mechanism of nonplanar growing interfaces. Since the mechanism we identify relies only on bulk transport processes, it is clear that interfacial energy is not the main contributor to interfacial stability in this

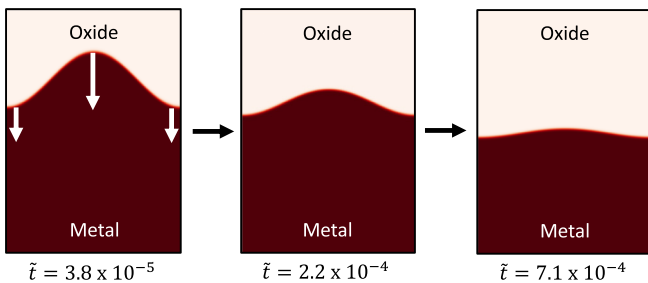


FIG. 10. Morphological change during inward oxidation in two dimensions. The perturbed, nonplanar interface becomes a planar one during growth.

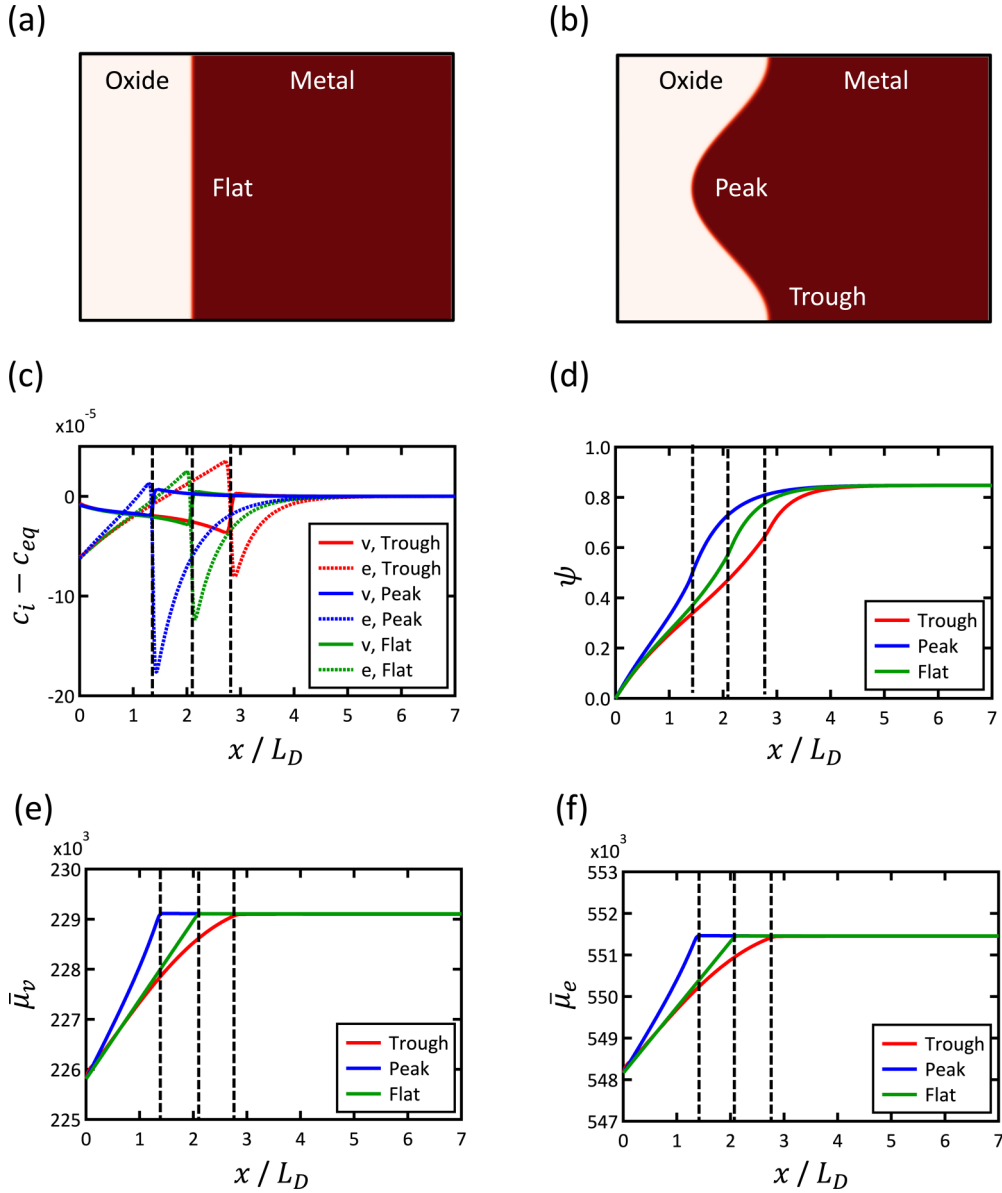


FIG. 11. Schematics of (a) flat and (b) perturbed interfaces. (c) The nondimensional concentration profiles of vacancies c_v and electrons c_e relative to c_{eq} , (d) electrostatic potential, ψ , profiles, electrochemical potential, $\bar{\mu}_i$, profiles of (e) vacancy and (f) electron across the trough and peak of a curved interface, and a flat interface. The dotted lines represent the location of the interface between the oxide and metal phases where ϕ is equal to 0.5.

case. This mechanism is consistent with the “self-stabilizing or self-healing” of a planar interface due to nonuniform electrochemical potential gradients when local equilibrium holds at the interface [6]. We studied a basic two-dimensional morphology with nonlinear periodic perturbations. Based on the current work, we will be able to simulate more complex morphologies (e.g., grain boundary) using multiorder parameters (phase-field variables) in the future.

IV. CONCLUSIONS

In this work, we have performed the phase-field modeling of oxidation. Based on our phase-field approach, we find the following:

(i) The phase-field model using a high interfacial mobility agrees with the Wagner parabolic growth law for diffusion-limited growth in the thick film limit where local equilibrium is satisfied at the gas-oxide and oxide-metal interfaces in the zero-charge limit.

(ii) Local equilibrium does not hold when the velocity of the interface becomes reaction limited. This occurs as the interfacial mobility is decreased. When the total oxidation reaction is controlled by the reaction at the interface, an electrostatic overpotential develops that results in linear growth kinetics during oxidation.

(iii) There is a transition in the kinetics of metal oxidation from a parabolic to linear growth rate depending on the value of the phase-field mobility. In the thin film limit where the

oxide phase is not charge neutral, the growth rate deviates more readily from the $t^{1/2}$ power than in the thick film limit for a given value of the phase-field mobility. In the low overpotential regime, the phase-field model yields a growth rate that is linearly proportional to the overpotential, consistent with Butler-Volmer kinetics.

(iv) For films with thicknesses less than the Debye length a concentration-dependent vacancy and electron mobility give rise to nonparabolic growth kinetics. However, for the material parameters employed in the simulations, the deviation from a parabolic growth law is small. As the film thickness increases and approaches a charge-neutral bulk film, this deviation becomes still smaller, and we recover parabolic kinetics.

(v) A perturbed nonplanar oxide-metal interface will eventually become planar during oxide growth. The phase-field method shows that the mechanism for the stabilization

of a planar interface is primarily the increase in growth rate of the peaks of the perturbation compared to the troughs, and not the interfacial energy.

ACKNOWLEDGMENTS

We acknowledge the support from the ONR MURI under Grant No. N00014-16-1-2280 and the computing resources from Quest high performance facility at Northwestern University. The authors thank Rohit Ramanathan for valuable discussions, and a reviewer of an earlier version of this paper for very helpful comments.

K.K. performed phase-field simulations using the open source MOOSE developed in INL, collaborated with Q.C.S. and L.K.A. K.K. and P.W.V. (overall leadership of project) wrote the manuscript.

The authors declare no competing interests.

-
- [1] X.-x. Yu, A. Gulec, Q. Sherman, K. L. Cwalina, J. R. Scully, J. H. Perepezko, P. W. Voorhees, and L. D. Marks, Nonequilibrium Solute Capture in Passivating Oxide Films, *Phys. Rev. Lett.* **121**, 145701 (2018).
- [2] M. Bobeth, W. Pompe, M. Rockstroh, and E. Schumann, Morphological instability of a planar oxide-alloy interface for inward oxide growth, *Acta Metall. Mater.* **42**, 579 (1994).
- [3] A. H. Heuer, T. Nakagawa, M. Z. Azar, D. B. Hovis, J. L. Smialek, B. Gleeson, N. D. M. Hine, H. Guhl, H. S. Lee, P. Tangney, W. M. C. Foulkes, and M. W. Finnis, On the growth of Al_2O_3 scales, *Acta Mater.* **61**, 6670 (2013).
- [4] C. Poulain, A. Seyeux, S. Voyshnis, and P. Marcus, Volatilization and transport mechanisms during Cr oxidation at 300 °C studied in situ by ToF-SIMS, *Oxid. Met.* **88**, 423 (2017).
- [5] C. Wagner, Beitrag zur theorie des anlaufvorgangs, *Z. Phys. Chem. B* **21**, 25 (1993).
- [6] H. Schmalzried, *Chemical Kinetics of Solids* (VCH, Weinheim, 1995).
- [7] A. Liebsch, Electronic screening at metal surfaces and the connection with physical phenomena, *Phys. Scr.* **35**, 354 (1987).
- [8] K. L. Kliewer and J. S. Koehler, Space charge in ionic crystals. I. General approach with application to NaCl, *Phys. Rev.* **140**, A1226 (1965).
- [9] N. Cabrera and N. F. Mott, Theory of the oxidation of metals, *Rep. Prog. Phys.* **12**, 163 (1949).
- [10] A. Atkinson, Transport processes during the growth of oxide films at elevated temperature, *Rev. Mod. Phys.* **57**, 437 (1985).
- [11] B. E. Deal and A. S. Grove, General relationship for the thermal oxidation of silicon, *J. Appl. Phys.* **36**, 3770 (1965).
- [12] R. E. Grace and T. F. Kassner, Transition kinetics during linear to parabolic oxidation of chromium, *Acta Metall.* **18**, 247 (1970).
- [13] L.-Q. Chen, Phase-field models for microstructure evolution, *Annu. Rev. Mater. Res.* **32**, 113 (2002).
- [14] N. Moelans, B. Blanpain, and P. Wollants, An introduction to phase-field modeling of microstructure evolution, *Calphad* **32**, 268 (2008).
- [15] Y.-H. Wen, L.-Q. Chen, and J. A. Hawk, Phase-field modeling of corrosion kinetics under dual-oxidants, *Modell. Simul. Mater. Sci. Eng.* **20**, 035013 (2012).
- [16] T.-L. Cheng, Y.-H. Wen, and J. A. Hawk, Diffuse-interface modeling and multiscale-relay simulation of metal oxidation kinetics—with revisit on Wagner’s theory, *J. Phys. Chem. C* **118**, 1269 (2014).
- [17] J. W. Cahn, On spinodal decomposition, *Acta Metall.* **9**, 795 (1961).
- [18] J. W. Cahn and J. E. Hilliard, Free energy of a nonuniform system. I. Interfacial free energy, *J. Chem. Phys.* **28**, 258 (1958).
- [19] M. Z. Bazant, Theory of chemical kinetics and charge transfer based on nonequilibrium thermodynamics, *Acc. Chem. Res.* **46**, 1144 (2013).
- [20] J. E. Guyer, W. J. Boettinger, J. A. Warren, and G. B. McFadden, Phase field modeling of electrochemistry. I. Equilibrium, *Phys. Rev. E* **69**, 021603 (2004).
- [21] J. E. Guyer, W. J. Boettinger, J. A. Warren, and G. B. McFadden, Phase field modeling of electrochemistry. II. Kinetics, *Phys. Rev. E* **69**, 021604 (2004).
- [22] Y. Shibuta, Y. Okajima, and T. Suzuki, Phase-field modeling for electrodeposition process, *Sci. Technol. Adv. Mater.* **8**, 511 (2007).
- [23] C. Lin and H. Ruan, Phase-field modeling of scale roughening induced by outward growing oxide, *Materialia* **5**, 100255 (2019).
- [24] Y. Okajima, Y. Shibuta, and T. Suzuki, A phase-field model for electrode reactions with Butler–Volmer kinetics, *Comput. Mater. Sci.* **50**, 118 (2010).
- [25] Y. Shibuta, Y. Okajima, and T. Suzuki, A phase-field simulation of bridge formation process in a nanometer-scale switch, *Scr. Mater.* **55**, 1095 (2006).
- [26] Q. C. Sherman and P. W. Voorhees, Phase-field model of oxidation: Equilibrium, *Phys. Rev. E* **95**, 032801 (2017).
- [27] R. A. Rapp, A. Ezis, and G. J. Yurek, Displacement reactions in the solid state, *Metall. Trans.* **4**, 1283 (1973).
- [28] R. Ramanathan and P. W. Voorhees, Morphological stability of steady-state passive oxide films, *Electrochim. Acta* **303**, 299 (2019).

- [29] R. F. Sekerka, S. R. Coriell, and G. B. McFadden, and Morphological stability, in *Handbook of Crystal Growth*, 2nd ed., edited by T. Nishinaga (Elsevier, Boston, 2015), Chap. 14, pp. 595–630.
- [30] D. Du and D. Srolovitz, Electrostatic field-induced surface instability, *Appl. Phys. Lett.* **85**, 4917 (2004).
- [31] D. J. Srolovitz, On the stability of surfaces of stressed solids, *Acta Metall.* **37**, 621 (1989).
- [32] B. J. Spencer, P. W. Voorhees, and S. H. Davis, Morphological instability in epitaxially strained dislocation-free solid films: Linear stability theory, *J. Appl. Phys.* **73**, 4955 (1993).
- [33] K.-A. Wu and P. W. Voorhees, Morphological instability of ferromagnetic thin films, *J. Appl. Phys.* **106**, 073916 (2009).
- [34] E. Schumann, G. Schnotz, K. P. Trumble, and M. Rühle, Microstructural observations on the oxidation of γ' -Ni₃Al at low oxygen partial pressure, *Acta Metall. Mater.* **40**, 1311 (1992).
- [35] A. T. Fromhold, Parabolic oxidation of metals in homogeneous electric fields, *J. Phys. Chem. Solids* **33**, 95 (1972).
- [36] A. Couet, A. T. Motta, and A. Ambar, The coupled current charge compensation model for zirconium alloy fuel cladding oxidation: I. Parabolic oxidation of zirconium alloys, *Corros. Sci.* **100**, 73 (2015).
- [37] J. W. Cahn and S. M. Allen, A microscopic theory for domain wall motion and its experimental verification in Fe-Al alloy domain growth kinetics, *J. Phys., Colloq.* **38**, C7-51 (1977).
- [38] S. G. Kim, W. T. Kim, and T. Suzuki, Phase-field model for binary alloys, *Phys. Rev. E* **60**, 7186 (1999).
- [39] D. Gaston, C. Newman, G. Hansen, and D. Lebrun-Grandié, MOOSE: A parallel computational framework for coupled systems of nonlinear equations, *Nucl. Eng. Des.* **239**, 1768 (2009).
- [40] D. Schwen, L. K. Aagesen, J. W. Peterson, and M. R. Tonks, Rapid multiphase-field model development using a modular free energy based approach with automatic differentiation in MOOSE/MARMOT, *Comput. Mater. Sci.* **132**, 36 (2017).
- [41] See Supplemental Material at <http://link.aps.org/supplemental/10.1103/PhysRevE.101.022802> for electrochemical potential profiles of defects across the oxide-metal interface for different sets of mobilities.
- [42] A. T. Fromhold, *Theory of Metal Oxidation* (North Holland Publishing Company, Amsterdam, 1976).
- [43] C. Wagner, Oxidation of alloys involving noble metals, *J. Electrochem. Soc.* **103**, 571 (1956).
- [44] N. Sridhar, J. M. Rickman, and D. J. Srolovitz, Microstructural stability of stressed lamellar and fiber composites, *Acta Mater.* **45**, 2715 (1997).